SIAM J. SCI. COMPUT.
Vol. 30, No. 3, pp. 1413–1429

LIMITED DATA X-RAY TOMOGRAPHY USING NONLINEAR EVOLUTION EQUATIONS*

VILLE KOLEHMAINEN†, MATTI LASSAS‡, AND SAMULI SILTANEN§

Abstract. A novel approach to the X-ray tomography problem with sparse projection data is proposed. Nonnegativity of the X-ray attenuation coefficient is enforced by modelling it as $\max\{\Phi(x), 0\}$, where Φ is a smooth function. The function Φ is computed as the equilibrium solution of a nonlinear evolution equation analogous to the equations used in level set methods. The reconstruction algorithm is applied to (a) simulated full and limited angle projection data of the Shepp–Logan phantom with sparse angular sampling and (b) measured limited angle projection data of in vitro dental specimens. The results are significantly better than those given by traditional backprojection-based approaches, and similar in quality (but faster to compute) compared to the algebraic reconstruction technique.

Key words. limited angle tomography, X-ray tomography, level set, nonlinear evolution equation

AMS subject classifications. 44A12, 92C55, 65N21, 65R32

DOI. 10.1137/050622791

1. Introduction.

In medical X-ray tomography, the inner structure of a patient is reconstructed from a collection of projection images. The widely used computerized tomography (CT) imaging uses an extensive set of projections acquired from all around the body. Reconstruction from such complete data is by now well understood, the most popular method being filtered backprojection (FBP).

However, there are many clinical applications where three-dimensional (3D) information is helpful, but a complete projection data set is not available. For example, in mammography and intraoral dental imaging, the X-ray detector is in a fixed position behind the tissue, and the X-ray source moves with respect to the detector. In these cases the projections can be taken only from a view angle significantly less than 180°, leading to a limited angle tomography problem. In some applications, such as surgical imaging, projections are available from all around the body, but the radiation dose to the patient is minimized by keeping the number of projections small. In addition, the projections are typically truncated to detector size, leading to a local tomography problem. We refer to the above types of incomplete data as *sparse projection data*.

Sparse projection data does not contain sufficient information to completely describe the tissue, and thus successful reconstruction requires some form of regularization or a priori information. It is well known that traditional reconstruction methods, such as FBP, are not well suited for sparse projection data [27, 20]. More promising

*Received by the editors January 17, 2005; accepted for publication (in revised form) July 16, 2007; published electronically April 9, 2008. This work was supported by National Technology Agency of Finland (TEKES, contract 206/03), the Academy of Finland (projects 203985 and 108299), and Finnish Centre of Excellence in Inverse Problems Research (Academy of Finland CoE-project 213476).

http://www.siam.org/journals/sisc/30-3/62279.html

†Department of Physics, University of Kuopio, P.O. Box 1627, 70211 Kuopio, Finland (ville.kolehmainen@uku.fi).

‡Institute of Mathematics, Helsinki University of Technology, P.O. Box 1100, 02015 TKK, Finland (matti.lassas@tkk.fi).

§Institute of Mathematics, Tampere University of Technology, P.O. Box 553, 33101 Tampere, Finland (samuli.siltanen@tut.fi).

approaches include algebraic reconstruction (variants of the algebraic reconstruction technique (ART)) [1, 5, 25], tomosynthesis [8], total variation methods [15, 24, 7, 6], Bayesian inversion [13, 30, 33, 15, 28, 17], variational methods [16], and deformable models [12, 3, 10, 42, 19].

We introduce a novel variant of the level set method, where the X-ray attenuation coefficient is modelled as the function $\max\{\Phi(x), 0\}$ with Φ a smooth function. Thus we make use of the natural a priori information that the X-ray attenuation coefficient is always nonnegative (the intensity of X-rays does not increase inside tissue).

We assume that the attenuation coefficient $v \in L^2(\Omega)$ for a bounded subset $\Omega \subset \mathbb{R}^2$ and use the following linear model for the direct problem:

$$m = Av + \varepsilon, \tag{1.1}$$

where A is a linear operator on $L^2(\Omega)$ with appropriate target space and ε is measurement noise. To reconstruct v approximately from m, we solve numerically the evolution equation

$$\begin{aligned} &\partial_t \phi(x,t) = -A^*(A(f(\phi(x,t))) - m) + \beta \Delta \phi(x,t), \\ &(\nu \cdot \nabla - r)\phi(x,t)|_{\partial\Omega} = 0, \end{aligned} \tag{1.2}$$

with a suitable initial condition $\phi(0) = \phi_0$ and $r \geq 0$, $\beta > 0$. Here ν is the interior normal vector of the boundary. The cutoff function $f : \mathbb{R} \to \mathbb{R}$ is given by

$$f(s) = \begin{cases} s, & s > 0, \\ 0, & s \leq 0. \end{cases} \tag{1.3}$$

We denote

$$\Phi(x) := \lim_{t \to \infty} \phi(x,t), \tag{1.4}$$

and consider the function

$$w(x) = f(\Phi(x)) \tag{1.5}$$

as the reconstructed attenuation coefficient.

The main difference between traditional level set methods [22, 31, 9, 29, 23, 36, 40] and our algorithm is that we represent the attenuation coefficient as $f(\Phi)$, as opposed to the traditional form $H(\Phi)$ with H the Heaviside function. Using f means that *the attenuation coefficient is represented by the smooth level set function itself in the regions bounded by zero level sets;* in classical level set methods the attenuation coefficient would be constant in those regions. In our experiments related to dental radiology, using f produces high quality reconstructions, whereas using H and piecewise constant representation leads to unacceptable quality.

In addition to computational results, we provide proofs of some aspects of our method. In Theorem 4.1 we show that the solution of the evolution equation (1.2) exists when the measurement equation (1.1) comes from one of the two most popular models for X-ray tomography: the pencil beam model or the Radon transform. Further, by Theorem 4.2 we know that the limit (1.4) exists when β is large enough and $r > 0$. While the proofs of the theorems rest on rather standard theory of nonlinear evolution equations, the novelty of our results lies in the combination of good reconstructions from measured data and theoretical justification for the proposed algorithm. The proofs rely essentially on the use of f instead of H.

Let us review earlier relevant level set studies. There are some approaches avoiding the Heaviside function but retaining the piecewise constant representation [18, 35]. Feng, Karl, and Castañon [10] show tomographic reconstructions with smooth variation from simulated noisy limited-view Radon transformed data. Yu and Fessler [42] use pixel-based representation inside components defined by level sets and an alternating minimization algorithm (our method simultaneously recovers the level sets and the interior). Villegas et al. [37] use Heaviside function and level sets for piecewise smooth geological inversion. A rigorous existence and uniqueness proof for the solution is given by Nguyen and Hoppe [21] in the context of amorphous surface growth.

This paper is organized as follows. In section 2 we discuss the pencil beam model and the Radon transform. Equation (1.2) is derived in section 3, and the solution is shown to converge to a nonnegative reconstruction of the attenuation coefficient in section 4. Reconstructions from sparse projection data, both simulated and measured (in vitro), are presented in section 5. We conclude our results in section 6.

2. X-ray measurement models. In medical X-ray imaging, an X-ray source is placed on one side of the target tissue. Radiation passes through the tissue, and the attenuated signal is detected on the other side; see the left-hand illustration in Figure 2.1.

We model a two-dimensional (2D) slice through the target tissue by a rectangle $\Omega \subset \mathbb{R}^2$ and a nonnegative attenuation coefficient $v : \Omega \to [0, \infty)$. The tissue is contained in a subset $\Omega_1 \subset \Omega$, and $v(x) \equiv 0$ for $x \in \Omega \setminus \Omega_1$. This leads to the linear model

$$\int_L v(x)\,dx = \log I_0 - \log I_1, \tag{2.1}$$

where L is the line of the X-ray, I_0 is the initial intensity of the X-ray beam when entering Ω, and I_1 is the attenuated intensity at the detector.

Below we present two popular ways to organize and interpret collections of measured line integrals (2.1) in the form (1.1): the *Radon transform* and the *pencil beam model*. We neglect scattering phenomena and effects of nonmonochromatic radiation, or beam hardening.

2.1. Radon transform. We define the operator A appearing in (1.1) by

$$A : L^2(\Omega) \to L^2(D), \qquad (Av)(\theta, s) = \int_{L(\theta,s)} v(x)\,dx,$$

where $L(\theta, s) = \{x \in \mathbb{R}^2 \,:\, x_1 \cos\theta + x_2 \sin\theta = s\}$. We allow models of limited angle and local tomography by taking

$$D = \{(\theta, s) \,:\, \theta \in [\theta_0, \theta_1], \quad s \in [s_0(\theta), s_1(\theta)]\},$$

where $0 \le \theta_0 < \theta_1 \le 2\pi$ and $-\infty \le s_0(\theta) < s_1(\theta) \le \infty$. Further, we assume that $\varepsilon \in L^2(D)$. We remark that A is a compact operator; see [20].

2.2. Pencil beam model. Suppose we take N_1 projection images with a digital detector consisting of N_2 pixels. Then our data consists of integrals of v over $N := N_1 N_2$ different lines L in (2.1). Accordingly, the linear operator in (1.1) is defined as

$$A : L^2(\Omega) \to \mathbb{R}^N,$$

the measurement is a vector $m \in \mathbb{R}^N$, and noise is modelled by a Gaussian zero-centered random vector ε taking values in $\mathbb{R}^N$.

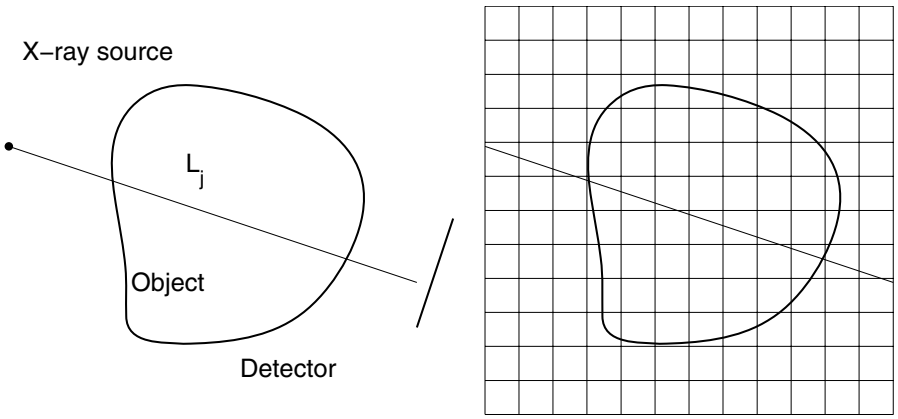

FIG. 2.1. *Left: typical measurement in X-ray transmission tomography. Right: in the discrete pencil beam model the domain Ω is divided into pixels.*

We remark that raw data in X-ray tomography consists of photon counts I_1 that obey Poisson statistics. However, a large number of photons are usually counted, and in addition, the projection data m represents the logarithm of the count data. It has been shown in [4, 33] that statistics of such data can be reasonably well approximated with the additive Gaussian noise model.

The pencil beam model needs to be discretized for practical computations. A square containing the domain Ω is divided into a lattice of disjoint pixels Ω_i with $i = 1, \ldots, M$. The attenuation map v is approximated by a constant value within each pixel:

$$v(x) \approx \sum_{i=1}^{M} v_i \chi_i(x), \tag{2.2}$$

where χ_i is the characteristic function of Ω_i. Using (2.2), the integral (2.1) can be approximated by the weighted sum of pixel values:

$$\int_L v(x)dx \approx \sum_{i=1}^{M} v_i \, \mu(\Omega_i \cap L), \tag{2.3}$$

where $\mu(\Omega_i \cap L)$ is the length of the line segment $\Omega_i \cap L$. See Figure 2.1 for an illustration. For discussion on different discretizations for the attenuation function $v(x)$ and approximations for the line integrals, see [14].

Furthermore, according to (2.2), the attenuation map can be identified with the coefficient vector $v = (v_1, v_2, \ldots, v_M)^{\mathrm{T}} \in \mathbb{R}^M$. Thus the discrete approximation to the operator A can be expressed as an $N \times M$ matrix with $CN\sqrt{M}$ nonzero entries.

We mention that computation of a discrete Radon transform can be done very effectively using algorithms given in [2] or in a matrix-free fashion utilizing graphic processing hardware; see, e.g., [41].

3. The evolution equation.

3.1. Classical level set method for inverse obstacle problems. Consider a physical parameter of the form $\sigma = \sigma_0 + c\chi_{\Omega_1}$, where $\sigma_0(x)$ is known background,

c is a constant, and the characteristic function $\chi_{\Omega_1}(x)$ causes a discontinuity at the boundary $\partial\Omega_1$. In inverse obstacle problems one aims to recover the set Ω_1 from indirect measurements of σ. For instance, the parameter σ may be sound speed or electrical impedance, and one may measure scattered waves or voltage-to-current boundary maps, respectively.

In the classical level set approach the obstacle is represented as $H(\Phi)$, where H is the Heaviside function and Φ is smooth. The boundary $\partial\Omega_1$ of the obstacle is given by the zero level set of Φ. The measurement is typically written in the form $m = A(H(\Phi)) =: Q(\Phi)$.

In the classical level set method the function Φ is found as the limit

$$\Phi(x) := \lim_{t\to\infty} \phi(x,t),$$

where ϕ is the solution of the evolution equation

$$\phi_t = -\theta(\phi, \nabla_x\phi)[(DQ|_\phi)^*(Q(\phi) - m)]. \tag{3.1}$$

Here θ is a nonnegative function and $(DQ|_\phi)\rho$ is the Gateaux derivative of Q at the point ϕ in direction $\rho \in C_0^\infty(\Omega)$ defined by

$$(DQ|_\phi)\rho = \lim_{s\to 0+} \frac{Q(\phi + s\rho) - Q(\phi)}{s}, \tag{3.2}$$

and $(DQ|_\phi)^*$ is the adjoint operator of $DQ|_\phi$.

The intuition behind this approach is the following. Define a cost functional

$$F_0(u) = \frac{1}{2}\|A(H(u)) - m\|^2_{L^2(D)} \tag{3.3}$$

and compute

$$\lim_{s\to 0+} \frac{\partial}{\partial s} F_0(u + s\rho) = \int_\Omega (DQ|_u)\rho\,(Q(u) - m)\,dx = \int_\Omega \rho\,(DQ|_u)^*(Q(u) - m)dx.$$

Then we have formally

$$\partial_t F_0(\phi) = \lim_{s\to 0+} \frac{\partial}{\partial s} F_0(\phi + s\phi_t) = -\int_\Omega \theta(\phi, \nabla_x\phi)\left[(DQ|_\phi)^*(Q(\phi) - m)\right]^2 dx \le 0,$$

and thus $\lim_{t\to\infty} F_0(\phi(x,t)) = F_0(\Phi)$ is expected to be small.

We refer the reader to [9] and the references therein for more details on solving inverse obstacle problems with classical level set methods.

3.2. Motivation for the new method. Consider the linear measurement (1.1) in the case that the X-ray attenuation coefficient v is smooth and differs from zero only inside a subset $\Omega_1 \subset \Omega$. Now the operator A^*A arising from the Radon transform or pencil beam model is nonlocal, and mathematical justification of the classical level set approach described in section 3.1 seems difficult. Also, our numerical experiments suggest that the classical level set method does not give satisfactory reconstructions when applied to the tomographic data available to us.

We want to design an algorithm that

(i) constructs an approximation Ω_2 for the subset Ω_1, and

(ii) with *given* approximation Ω_2 produces a reconstruction w that solves the Tikhonov regularization problem

$$w = \arg\min_u \left\{ \frac{1}{2}\|A(u) - m\|^2_{L^2(D)} + \frac{\beta}{2}\|\nabla u\|^2_{L^2(\Omega)} \right\},$$

where $\beta > 0$ is a parameter and the minimum is taken over all u satisfying

$$u|_{\Omega\setminus\Omega_2} \equiv 0, \tag{3.4}$$

$$u|_{\Omega_2} \in H^1_0(\Omega_2) = \{g \in L^2(\Omega_2) :\ \nabla g \in L^2(\Omega_2),\ g|_{\partial\Omega_2} = 0\}. \tag{3.5}$$

However, goal (ii) depends on goal (i). One possibility overcoming this problem would be to iteratively alternate between (i) and (ii) similarly to [42], but we follow another route.

3.3. Formulation of the new method. We approximate the X-ray attenuation coefficient v by $w = f(\Phi)$, where f is given by (1.3) and Φ is smooth. Note that (3.4) is achieved naturally with $\partial\Omega_2$ given by the zero level set of Φ. The measurement of X-ray projection images is now modelled by $m = A(f(\Phi))$.

In the new method the function Φ is found as the limit $\Phi(x) := \lim_{t\to\infty} \phi(x,t)$, where ϕ is the solution of the evolution equation

$$\begin{aligned} &\partial_t \phi = -(A^*(A(f(\phi)) - m)) - \beta\Delta\phi, \\ &\partial_\nu \phi - r\phi|_{\partial\Omega} = 0, \\ &\phi(x,0) = \phi_0(x), \end{aligned} \tag{3.6}$$

with ν the interior normal of $\partial\Omega$, $\beta > 0$ a regularization parameter, and $r \geq 0$. Compare (3.6) to (3.1) with the choice $\theta \equiv 1$.

The function w in goals (i) and (ii) of section 3.2 satisfies

$$\beta\Delta w - A^*(A(w) - m) = 0 \qquad \text{in } \Omega_2. \tag{3.7}$$

The solution of evolution equation (3.6) converges to the solution of (3.7) and *simultaneously* produces a useful approximation Ω_2 for Ω_1. Note that since the result of the evolution is nonnegative, it follows from (3.7) that w in goals (i) and (ii) is nonnegative as well.

How did we come up with such a formulation? Tikhonov regularization leads to the cost functional

$$F(u) = \frac{1}{2}\|A(f(u)) - m\|^2_{L^2(D)} + \frac{\beta}{2}\|\nabla u\|^2_{L^2(\Omega)}. \tag{3.8}$$

Computing the derivative $\partial_t F(u)$ similarly to the process in section 3.1 suggests the evolution

$$\partial_t \phi = -H(\phi)(A^*(A(f(\phi)) - m)) - \beta\Delta\phi. \tag{3.9}$$

However, (3.9) is numerically unstable. Outside the level set $\Omega_2(t) := \{x \,|\, \phi(x,t) = 0\}$ the evolution is driven by the term $-\beta\Delta\phi$ alone, pushing ϕ typically toward constant value zero in $\Omega \setminus \Omega_2$. This in turn creates spurious and unstable components of the level set Ω_2.

Thus we drop the Heaviside function in (3.9) and arrive at (3.6). Numerical tests show that evolution (3.6) is numerically stable and gives much better reconstructions than (3.9).

4. Existence proof for the new method. In the following theorem we show that (3.6) has a strong $L^2(\Omega)$ solution. We remark that similar analysis fails for the classical level set approach because using H instead of f leads to a heat equation with very singular source terms.

THEOREM 4.1. *Let $A : L^2(\Omega) \to L^2(D)$ and $m \in L^2(D)$, where D is either a subset of $\mathbb{R}^2$ equipped with the Lebesgue measure, or $D = \{1, 2, \ldots, N\}$ equipped with the counting measure. Assume $\phi_0 \in W^{1,2}(\Omega)$, $r \geq 0$, and $\beta > 0$.*

Then the evolution equation,

$$\partial_t \phi = -A^*(A(f(\phi)) - m) + \beta \Delta \phi \quad \text{in } \Omega \times \mathbb{R}_+, \tag{4.1}$$

$$(\partial_\nu - r)\phi|_{\partial\Omega} = 0, \tag{4.2}$$

$$\phi(x, 0) = \phi_0(x), \tag{4.3}$$

has a solution $\phi \in W^1([0, T]; L^2(\Omega)) \cap L^2([0, T]; H^1(\Omega))$ for any $T > 0$.

Remark. The assumptions of Theorem 4.1 are satisfied when A is the Radon transform (including limited angle and local tomography cases). Further, $\mathbb{R}^N$ can be identified with the space $L^2(D)$ when $D = \{1, 2, \ldots, N\}$ equipped with the counting measure. This way we see that Theorem 4.1 covers the pencil beam model as well.

Proof. We consider first the equation on a finite time interval $[0, T]$. We denote

$$B(\phi) = A^* A(f(\phi)), \quad g = A^* m.$$

Let $\psi(x, t) = e^{-\eta t}\phi(x, t)$, $\eta \geq 0$. Since $f(sa) = sf(a)$ for $s > 0$, (4.3) is equivalent to

$$\partial_t \psi = [-\eta\psi - A^* A(f(\psi)) + \beta\Delta\psi] + g, \tag{4.4}$$

$$\psi(x, 0) = \phi_0,$$

$$(\partial_\nu - r)\psi|_{\partial\Omega} = 0, \tag{4.5}$$

for $t \in [0, T]$. Next we consider this equation.

Let $V = W^{1,2}(\Omega)$ be the Sobolev space and V' its dual. Then V is separable and reflexive, and the embedding $V \to L^2(\Omega)$ is compact. In the following, Δ is always the Laplacian defined with Robin boundary condition $(\partial_\nu - r)\phi|_{\partial\Omega} = 0$. This operator has a continuous extension $\Delta : V \to V'$. Let $\lambda_0 \geq 0$ be the smallest Robin eigenvalue of $-\Delta$ in Ω.

We choose the value of η such that for some $\varepsilon_1, \varepsilon_2 > 0$

$$\|A^* A\|_{L(L^2(\Omega))} \leq \eta + (\beta - \varepsilon_2)\lambda_0 - \varepsilon_1.$$

First, since $\|f(u)\|_{L^2(\Omega)} \leq \|u\|_{L^2(\Omega)}$ and $A^* A : L^2(\Omega) \to L^2(\Omega)$ is continuous, we observe that the operator $u \mapsto \beta\Delta u + B(u)$ is hemicontinuous $V \to V'$, that is, for any $u, v \in V$ the map

$$s \mapsto \langle \beta\Delta(u + sv) + B(u + sv), v\rangle$$

is continuous from $\mathbb{R}$ to $\mathbb{R}$. Also, it satisfies an estimate

$$\|\beta\Delta(u) + B(u)\|_{V'} \leq c_3 \|u\|_V. \tag{4.6}$$

Because of the choice of η, we have that

$$\langle \eta u + B(u), u\rangle \geq (\varepsilon_1 - (\beta - \varepsilon_2)\lambda_0)\|u\|^2_{L^2(\Omega)}. \tag{4.7}$$

Since Δ is defined with Robin boundary conditions, we see that

$$\langle(-\Delta u), u\rangle \geq \lambda_0 \|u\|^2_{L^2(\Omega)}.$$

Using (4.7) we see that

$$\begin{aligned}\langle -\beta\Delta u + B(u) + \eta u, u\rangle &\geq \langle(-\varepsilon_2\Delta u), u\rangle + \langle(\varepsilon_2 - \beta)\Delta u + B(u) + \eta u, u\rangle \\ &\geq \varepsilon_2 \|\nabla u\|^2_{L^2(\Omega)} + \varepsilon_1 \|u\|^2_{L^2(\Omega)} \\ &\geq \min(\varepsilon_1, \varepsilon_2)\, \|u\|^2_V.\end{aligned} \tag{4.8}$$

Since $|f(s_1) - f(s_2)| \leq |s_1 - s_2|$ and $A^*A : L^2(\Omega) \to L^2(\Omega)$ is continuous, we have

$$|\langle B(u_1) - B(u_2), u_1 - u_2\rangle| \leq \|A^*A\|_{L(L^2(\Omega))}\, \|u_1 - u_2\|^2_{L^2(\Omega)}, \tag{4.9}$$

$$\langle(\eta - \beta\Delta)(u_1 - u_2), u_1 - u_2\rangle \geq (\eta + R\lambda_0)\|u_1 - u_2\|^2_{L^2(\Omega)}. \tag{4.10}$$

Thus the operator $\mathcal{A}u = -\beta\Delta u + B(u) + \eta u$ is hemicontinuous and satisfies

$$\begin{aligned}\langle \mathcal{A}(u_1) - \mathcal{A}(u_2), u_1 - u_2\rangle &\geq (\eta + \beta\lambda_0 - \|A^*A\|_{L(L^2(\Omega))})\|u_1 - u_2\|^2_{L^2(\Omega)} \\ &\geq \varepsilon_1 \|u_1 - u_2\|^2_{L^2(\Omega)}.\end{aligned} \tag{4.11}$$

This means by definition that $\mathcal{A}$ is a strictly monotone operator.

Thus we have shown that $\mathcal{A}(\,\cdot\,)$ is a hemicontinuous and satisfies (4.6), (4.8), and (4.11). Hence all assumptions of the existence theorem [32, Prop. III.4.1] concerning quasilinear parabolic equations are valid (see also [32, Lemma II.2.1]), and we see that (4.3) has a unique solution in the weak sense on any time interval $[0, T]$ and thus on $t \in \mathbb{R}_+$; that is, $\psi \in C([0, T]; L^2(\Omega)) \cap L^2(0, T; V)$, $\partial_t\psi \in L^2(0, T; V')$, and for any $u \in C([0, T]; L^2(\Omega)) \cap L^2(0, T; V)$ with $u(T) = 0$ we have

$$\begin{aligned}&-\int_0^T \langle \partial_t\psi(t), u(t)\rangle_{V'\times V}\, dt + \int_0^T \langle \mathcal{A}(\psi(t)), u(t)\rangle_{V'\times V}\, dt \\ &= \int_0^T \langle g(t), u(t)\rangle_{L^2(\Omega)\times L^2(\Omega)}\, dt + \langle \phi_0, v(0)\rangle_{L^2(\Omega)\times L^2(\Omega)}.\end{aligned}$$

Next we show that ψ is a strong solution. Observe that $\psi(t)$ is a weak solution of the linear equation

$$\partial_t\psi(t) + \eta\psi - \beta\Delta\psi(t) = \widetilde{g}(t), \quad \psi(0) = \phi_0, \quad (\partial_\nu - r)\psi|_{x\in\partial M} = 0, \tag{4.12}$$

where $\widetilde{g} = B(\psi(t)) + g \in C([0, T]; L^2(\Omega))$. Using (4.12) we see by [32, Prop. III.4.2] that $\psi \in L^\infty(0, T; V)$, $\partial_t\psi \in L^2(0, T; L^2(\Omega))$, and in $L^2(\Omega)$ we have

$$\partial_t\psi(t) = -\eta\psi(t) + \beta\Delta\psi(t) + \widetilde{g}(t) = \mathcal{A}(\psi(t)) + g(t) \quad \text{for a.e. } t \in [0, T]. \qquad \square$$

Next we show that the limit $\lim_{t\to\infty} \phi(x, t)$ exists for $r > 0$ and large β.

THEOREM 4.2. *Let A and m be as in Theorem* 4.1. *Let ϕ be the solution of* (4.1) *with $r > 0$. Then there is $\beta_0 > 0$ depending on Ω and A such that if $\beta > \beta_0$, then the limit*

$$\Phi(x) := \lim_{t\to\infty} \phi(x, t)$$

exists in the topology of $L^2(\Omega)$ *and* Φ *is a solution of the equation*

$$A^*A(f(\Phi)) - \beta\Delta\Phi = A^*m \quad \text{in } \Omega, \qquad (\partial_\nu - r)\Phi|_{\partial\Omega} = 0. \tag{4.13}$$

Proof. Recall that $\mathcal{A}u = -\beta\Delta u + B(u) + \eta u$. Since $\mathcal{A} : V \to V'$ is strictly monotone and hemicontinuous and satisfies (4.6) and (4.8), it follows from [32, Thm. II.2.1 and Lemma II.2.1] that the equation

$$\mathcal{A}(\Phi) = g, \quad \Phi \in V, \tag{4.14}$$

has a unique solution.

Denote $S_1(u) = \langle \mathcal{A}(u+\Phi) - \mathcal{A}(\Phi), u\rangle$. Then $S_1(u-\Phi) = \langle \mathcal{A}(u) - m, u - \Phi\rangle$. By (4.8) we see that

$$-S_1(u-\Phi) \geq \min(\varepsilon_1, \varepsilon_2)\|u-\Phi\|_V^2. \tag{4.15}$$

Now for a.e. $t \in \mathbb{R}_+$ we have for the solution $\psi(t)$ of (4.12)

$$\begin{aligned}\partial_t(\|\psi(t)-\Phi\|^2_{L^2(\Omega)}) &= 2\langle \partial_t\psi(t), \psi(t)-\Phi\rangle \\ &= 2\langle -\mathcal{A}(\psi(t)) + g, \psi(t)-\Phi\rangle \\ &= -2S_1(\psi(t)-\Phi),\end{aligned}$$

and, denoting $\varepsilon_3 = \min(\varepsilon_1, \varepsilon_2)$, we see that

$$\partial_t(\|\psi(t)-\Phi\|^2_{L^2(\Omega)}) \leq -\varepsilon_3\|\psi(t)-\Phi\|^2_{L^2(\Omega)}.$$

Thus $s(t) = \|\psi(t)-\Phi\|^2_{L^2(\Omega)}$ satisfies $s(t) \leq s(0)\exp(-\varepsilon_3|t-t_1|)$, implying that

$$\|\psi(t)-\Phi\|_{L^2(\Omega)} \leq \|\psi(0)-\Phi\|_{L^2(\Omega)}\exp(-\varepsilon_1|t-t_1|).$$

Finally, when β is large enough, we can choose $\eta = 0$. Then $\phi(t) = \psi(t)$, and the claim follows. ∎

5. Computational results. We test the proposed method with simulated and measured projection data. The first test case is a simulated example of full angle and limited angle tomography with sparse projection data from the classical Shepp–Logan phantom. With the full angle data we study the effect of angular sampling on reconstruction quality. Results with FBP and ART are given as references. For details on FBP, see [14, 20], and for details on ART, see [1, 5, 25].

The second test case is limited angle tomography with data measured from a tooth specimen, and the third test case uses intraoral projection data from a dry skull. In these cases, reconstructions with the traditional tomosynthetic method are shown as reference. Tomosynthesis, or unfiltered backprojection, is widely used for dental imaging with few projections; see [38, 11, 39].

We use 2D discrete pencil beam model in all computations. We discretize the evolution equation (4.3) using a finite difference scheme where $\phi(x, t_k)$ is approximated with the piecewise constant function

$$\phi(x, t_k) \approx \sum_{i=1}^{M} \phi_i(t_k)\chi_i(x) \tag{5.1}$$

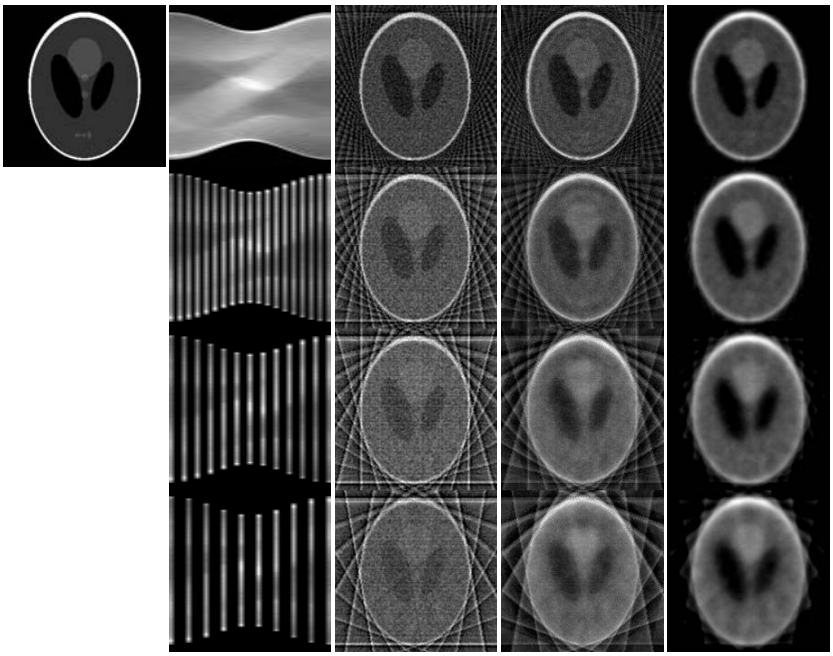

FIG. 5.1. *Simulated sparse full angle projection data from the Shepp–Logan phantom. First column from the left: the Shepp–Logan phantom. Second column: data in sinogram form. In all cases the total view angle is* 180°. *The number of projections from top to bottom is* 37 *(*5° *step),* 19 *(*10°*),* 13 *(*15°*), and* 10 *(*20°*), respectively. The missing parts of the sinograms are denoted by black. Third column: reconstructions with FBP. Fourth column: reconstructions with ART. Fifth column: reconstructions with the proposed method. See Table* 5.1 *for relative errors of the reconstructions and the computation times.*

and central differencing is used for the computation of the partial derivatives. Homogeneous Neumann boundary condition $\nabla\phi\cdot\nu = 0$ is used at the exterior boundary $\partial\Omega$. For temporal discretization we employ an explicit Euler method. 3D reconstructions are formed as stacks of reconstructed 2D slices.

The computations are carried out using MATLAB 7.1 on a modern desktop computer (3.2GHz Pentium 4 processor with 4GB random access memory).

5.1. Full and limited angle tomography with sparse angular sampling. We simulate projection data using the Shepp–Logan phantom of size 256×256 shown in Figure 5.1. Using the conventional parallel beam CT imaging geometry, 37 one-dimensional projections from a total view angle of 180° (with 5° steps) are generated. The number of line integrals in each projection is 180, leading to a total number of data $N = 37 \times 180 = 6660$. Additive Gaussian noise with standard deviation 3% of the maximum value of the generated projections is added to the data, leading to a signal-to-noise ratio of 25 dB.

We divide the domain $\Omega \subset \mathbb{R}^2$ into $M = 180 \times 180 = 32400$ regular pixels. The smoothing parameter in the evolution equation is taken to be $\lambda = 0.1$. Table 5.1 shows the numbers of data we use. Figure 5.1 shows the full angle data in sinogram form and reconstructions from the respective data. The number of projections is from top to bottom 37, 19, 13, and 10, respectively. In FBP reconstructions we reduce the effects of noise by applying the Ram–Lak filter multiplied by the Hamming window to the filtering in the frequency domain and use the nearest neighbor interpolation

TABLE 5.1

Measurement parameters, relative L^2-errors, and computation times of the reconstructions given in Figure 5.1.

Number of projections	Angular step size	N	Error of FBP	Error of ART	Error of new method
37	5°	6660	60.7 %	44.4 %	48.8 %
19	10°	3420	85.9 %	52.4 %	54.3 %
13	15°	2340	107.4 %	58.1 %	57.7 %
10	20°	1800	127.0 %	62.1 %	60.5 %

Number of projections	Computation time of FBP	Computation time of ART	Computation time of new method
37	0.2 s	523.1 s	49.6 s
19	0.1 s	145.1 s	29.4 s
13	0.1 s	57.8 s	22.0 s
10	0.1 s	26.1 s	17.5 s

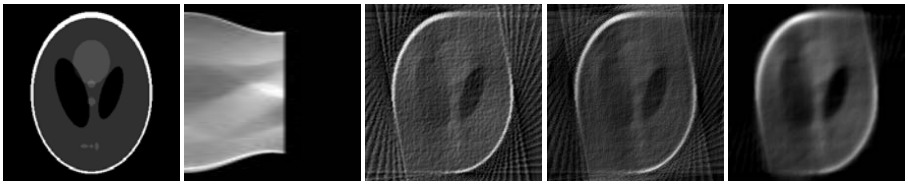

FIG. 5.2. *Simulated limited angle projection data from the Shepp–Logan phantom. First column from the left: the Shepp-Logan phantom. Second column: data in sinogram form. The data consisted of* 21 *projections with* 5° *steps, leading to a total opening angle of* 100°. *The missing parts of the sinogram are denoted by black. Third column: reconstruction with FBP. Fourth column: reconstruction with ART. Fifth column: reconstruction with the proposed method. See Table* 5.2 *for relative errors of the reconstructions and the computation times.*

TABLE 5.2

Measurement parameters, relative L^2-errors, and computation times of the limited angle reconstructions given in Figure 5.2. *The data consisted of* 21 *projections from a total opening angle of* 100° *(number of data* $N = 3780$*).*

	FBP	ART	New method
Error	90.3 %	65.6 %	61.6 %
Computation time	0.1 s	59.0 s	27.8 s

in the backprojection process. In the ART reconstructions, the iteration is terminated once the least squares residual reaches the expected level of the measurement noise. Table 5.1 contains the computation times and the relative L^2-errors of the reconstructions shown in Figure 5.1.

Figure 5.2 shows the results from the limited angle data which consisted of 21 projections with total opening angle of 100° (5° steps). The relative L^2-errors and computation times of the reconstructions are tabulated in Table 5.2.

5.2. Sparse limited angle data from a tooth specimen. We acquire projection images using full angle cone beam CT geometry, so full angle reconstructions are available as ground truth for the limited angle reconstructions.

We use a commercial intraoral X-ray detector Sigma and a dental X-ray source Focus.[1] The detector is based on charge coupled device technology. The size of the

[1]Sigma and Focus are registered trademarks of PaloDEx Group.

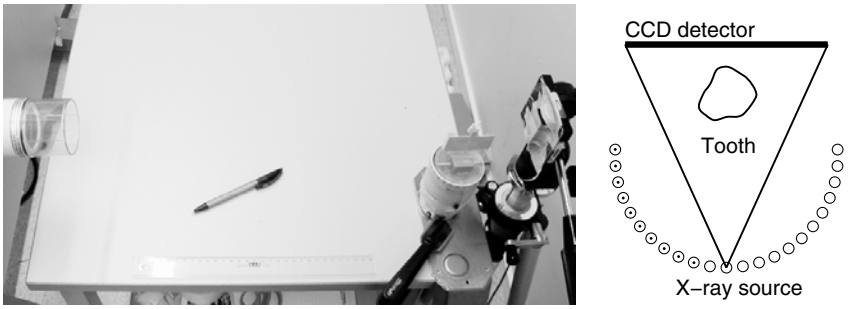

FIG. 5.3. *Left: the experimental setup. The X-ray source is on the left, and the detector is attached to the camera stand on the right. The tooth phantom is positioned on the rotating platform. Right: illustration of the projection geometry. Circles denote the source locations for the full angle data (*23 *projections from total view angle of* 187°*). The projections used in limited angle computations (*10 *projections from view angle of* 76°*) are denoted by black dots within the circles. For clarity, the location and alignment of the detector with respect to the source are depicted for only one source location.*

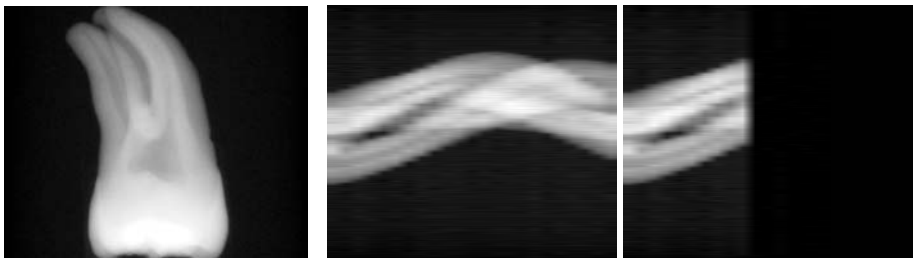

FIG. 5.4. *Left: projection radiograph of the tooth specimen. Note that the radiograph is shown with inverted color map. Middle: one* 2*D slice of the (transformed) projection data in sinogram form. The projections are collected from a total view angle of* 187° *(*23 *projections with* 8.5° *steps). Right: the part of data used in the limited angle reconstructions (*10 *projections from a total view angle of* 76°*). The missing part of the sinogram is denoted by black.*

imaging area is 34mm × 26mm, and the resolution is 872 × 664 pixels with pixel size 0.039mm × 0.039mm. Signal-to-noise ratio in our experiments is 34 dB.

In the experimental setup, the detector and the X-ray source are attached into fixed positions such that the source direction is normal to the detector array. The distance from the focal spot to the detector is 840mm. The tooth specimen is placed on a rotating platform so that projections from different angles can be obtained. The distance from the center of rotation to the detector is 56mm. Projection angles are read from a millimeter scale paper attached to the rotating platform. The measurement setup is illustrated in Figure 5.3.

We take 23 projection images from a total view angle of 187° (with 8.5° steps) and transform them into projection data of the form (2.1). We use two angular samplings: 23 projections from a total view angle of 187° and 10 projections from a total view angle of 76°. The size of the data vector m for each 2D problem is $N = 664 \times 23 = 15272$ in the full angle case and $N = 664 \times 10 = 6640$ in the limited angle case. Figure 5.4 shows one of the projection radiographs and one 2D slice of the projection data in sinogram form.

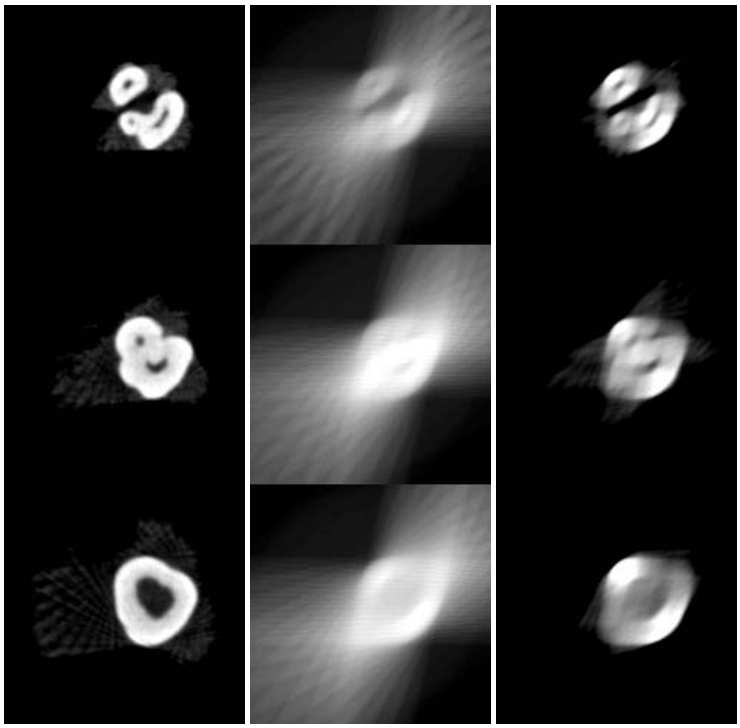

FIG. 5.5. *Left column: reconstructed slices from full angle data consisting of* 23 *projection images from a total view angle of* 187°. *Center column: backprojected reconstructions from limited angle data (*10 *projections from a total view angle of* 76°*). Right column: reconstructions with the proposed method from the same limited angle data. Relative* L^2*-errors from top to bottom:* 29%, 30%, *and* 40%.

We divide the 26mm × 26mm square domain $\Omega \subset \mathbb{R}^2$ into $M = 166 \times 166 = 27556$ regular pixels, leading to a pixel size of $\sim 0.16\text{mm} \times 0.16\text{mm}$. The smoothing parameter in the evolution equation is $\lambda = 0.1$. Results are shown in Figures 5.5 and 5.6.

5.3. Sparse intraoral data from a dry skull. We model intraoral X-ray imaging by placing the detector in a fixed position inside the mouth of a dry skull right behind the teeth. A metal reference ball is attached in front of the teeth with distance of 14mm from the detector for calibration. We move the X-ray source on an approximately circular arc with a distance of $\sim$ 590mm from the detector. A photograph and a schematic illustration of the experimental setup are shown in Figure 5.7.

We take seven projection images with approximately equal angular steps from a total view angle of 60°. This represents roughly the maximum view angle that can be used in practice. Projection angles are estimated based on the shift of the reference ball in the images. Figure 5.8 shows one projection radiograph from this data set and one slice of the data in sinogram form. Note that the sinogram is truncated from the upper side (i.e, it does not go to zero in the upper side). Thus, in addition of being a limited angle case, the problem contains features of a local tomography problem [34, 26].

The number of data for each 2D problem is $N = 872 \times 7 = 6104$, and the smoothness parameter in the evolution equation is $\lambda = 0.1$. The domain $\Omega \subset \mathbb{R}^2$ is

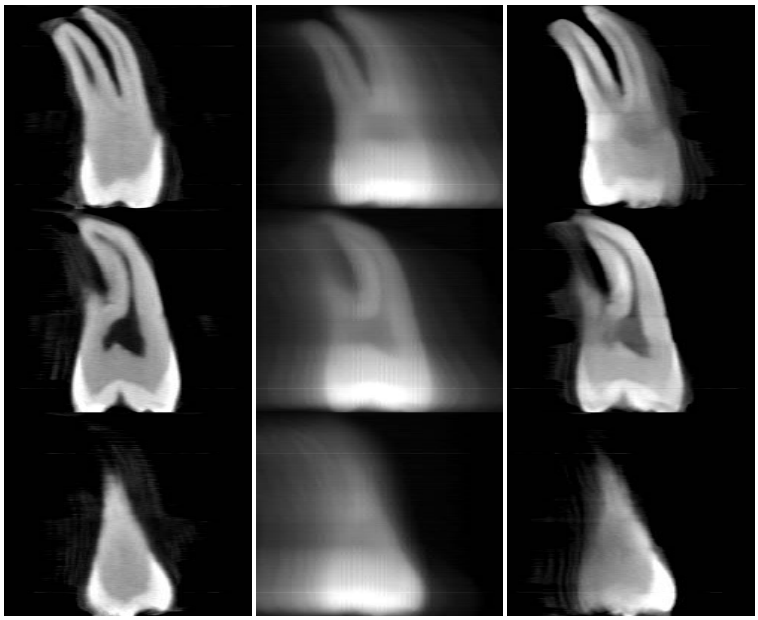

FIG. 5.6. *Vertical slices from* 3*D reconstructions obtained as stacks of* 2*D reconstructions. Left column: reconstruction from full angle data consisting of* 23 *projection images from a total view angle of* 187°. *Center column: backprojected reconstruction from limited angle data (*10 *projections from a total view angle of* 76°*). Right column: reconstruction with the proposed method from the same limited angle data.*

FIG. 5.7. *Left: geometry for intraoral measurements. The detector is in fixed position inside the patient's mouth. The source locations are denoted by black dots (*7 *projections from a total view angle of* 60°*). Right: experimental setup.*

a 61mm × 25mm rectangle divided into $M = 393 \times 160 = 62880$ regular pixels with size $\sim 0.16\text{mm} \times 0.16\text{mm}$. The results for the dry skull case are shown in Figure 5.9.

6. Conclusion. We introduce a novel reconstruction method for tomographic problems. Our approach is inspired by level set methods. The algorithm is given in the form of a nonlinear evolution equation, for which we prove existence of solutions and convergence to a limit function considered as the reconstruction.

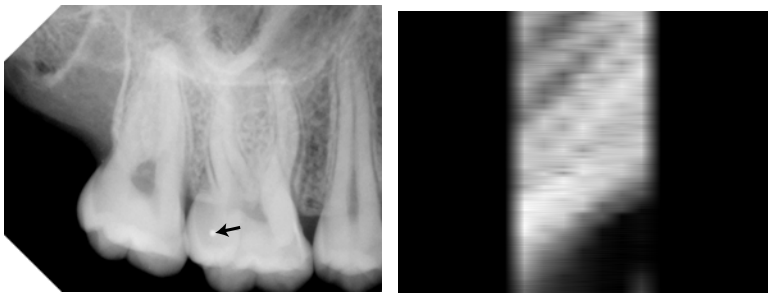

FIG. 5.8. *Left: Intraoral projection radiograph of the head phantom. The location of the image of the metal ball used to estimate the projection angles is indicated. Right: One* $2D$ *slice of data in sinogram form. The projections are collected from a total view angle of* $60°$*. The black parts denote the missing parts of the sinogram.*

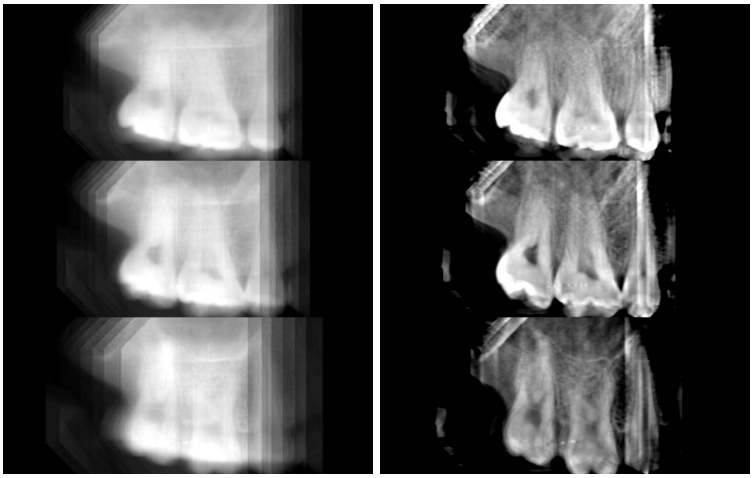

FIG. 5.9. *Approximate* $3D$ *reconstruction from limited angle projection data from the dry skull. The* $3D$ *reconstruction was obtained as a stack of* $2D$ *reconstructions. The data consists of* 7 *intraoral projection images collected from a total view angle of* $60°$*. Left column: vertical slices from a backprojected reconstruction. Right column: respective slices with the proposed method.*

Reconstructions computed from simulated full angle and limited angle data show that the proposed method clearly decreases the reconstruction error compared to FBP, and the reconstruction errors are similar to those of ART. The computation times of the new method are significantly smaller than those of ART.

Further, we perform realistic experiments involving specimens of dental tissue. The new method gives excellent results in all test cases as judged by visual inspection. Diagnostically crucial information, such as the position of tooth roots, is more clearly visible in the reconstructions using the new method than in tomosynthetic slices.

The new method is easy to implement, and the most computational effort goes to linear projection and backprojection operations (for which highly optimized hardware implementations are available).

One drawback of the proposed method is that the reconstruction $f(\Phi)$ is always a continuous function although the target tissue is known to have jumps in the attenuation coefficient.

REFERENCES

[1] A.H. Andersen, *Algebraic reconstruction in CT from limited views*, IEEE Trans. Med. Imaging, 8 (1989), pp. 50–55.

[2] A. Averbuch and Y. Shkolnisky, *3D Fourier based discrete Radon transform*, Appl. Comput. Harmon. Anal., 15 (2003), pp. 33–69.

[3] X. L. Battle, G. S. Cunningham, and K. M. Hanson, *3D tomographic reconstruction using geometrical models*, in Proceedings of SPIE 3034, Medical Imaging: Image Processing, K. M. Hanson, ed., 1997, pp. 346–357.

[4] C. Bouman and K. Sauer, *A generalized Gaussian image model for edge-preserving MAP estimation*, IEEE Trans. Image Process., 2 (1993), pp. 296–310.

[5] C. Byrne, *Block-iterative interior point optimization methods for image reconstruction from limited data*, Inverse Problems, 16 (2000), pp. 1405–1419.

[6] E. J. Candès, J. Romberg, and T. Tao, *Robust uncertainty principles: Exact signal reconstruction from highly incomplete frequency information*, IEEE Trans. Inform. Theory, 52 (2006), pp. 489–509.

[7] A. H. Delaney and Y. Bresler, *Globally convergent edge-preserving regularized reconstruction: An application to limited-angle tomography*, IEEE Trans. Image Process., 7 (1998), pp. 204–221.

[8] J. T. Dobbins and D. J. Godfrey, *Digital x-ray tomosynthesis: Current state of the art and clinical potential*, Phys. Med. Biol., 48 (2003), pp. R65–R106.

[9] O. Dorn and D. Lesselier, *Level set methods for inverse scattering*, Inverse Problems, 22 (2006), pp. R67–R131.

[10] H. Feng, W. C. Karl, and D. A. Castañon, *A curve evolution approach to object-based tomographic reconstruction*, IEEE Trans. Image Process., 12 (2003), pp. 44–57.

[11] D. G. Grant, *Tomosynthesis: A three-dimensional radiographic imaging technique*, IEEE Trans. Biomedical Engrg., 19 (1972), pp. 20–28.

[12] K. M. Hanson, G. S. Cunningham, G. R. Jennings, and D. R. Wolf, *Tomographic reconstruction based on flexible geometric models*, in Proceedings of the IEEE International Conference on Image Processing (ICIP-94), 1994, pp. 145–147.

[13] K. M. Hanson and G. W. Wecksung, *Bayesian approach to limited-angle reconstruction in computed tomography*, J. Opt. Soc. Amer., 73 (1983), pp. 1501–1509.

[14] A. C. Kak and M. Slaney, *Principles of Computerized Tomographic Imaging*, Classics Appl. Math. 33, SIAM, Philadelphia, 2001.

[15] V. Kolehmainen, S. Siltanen, S. Järvenpää, J. P. Kaipio, P. Koistinen, M. Lassas, J. Pirttilä, and E. Somersalo, *Statistical inversion for medical X-ray tomography with few radiographs:* II. *Application to dental radiology*, Phys. Med. Biol., 48 (2003), pp. 1465–1490.

[16] J. Kybic, T. Blu, and M. Unser, *Variational approach to tomographic reconstruction*, in Proceedings of SPIE (San Diego, 2001), Vol. 4322, Medical Imaging 2001: Image Processing, Milan Sonka, Kenneth M. Hanson, eds., 2001, pp. 30–39.

[17] M. Lassas and S. Siltanen, *Can one use total variation prior for edge-preserving Bayesian inversion?*, Inverse Problems, 20 (2004), pp. 1537–1563.

[18] J. Lie, M. Lysaker, X.-C. Tai, *A binary level set model and some applications to Mumford–Shah image segmentation*, IEEE Trans. Image Process., 15 (2006), pp. 1171–1181.

[19] A. Mohammad-Djafari and K. Sauer, *Shape reconstruction in x-ray tomography from a small number of projections using deformable models*, in Proceedings of the 17th International Workshop on Maximum Entropy and Bayesian Methods (MaxEnt97), Boise, ID, 1997.

[20] F. Natterer, *The Mathematics of Computerized Tomography*, John Wiley & Sons, Chichester, UK, Teubner, Stuttgart, 1986.

[21] C.-D. Nguyen and H. W. Hoppe, *Amorphous surface growth via a level set approach*, Nonlinear Anal., 66 (2007), pp. 704–722.

[22] S. Osher and R. Fedkiw, *Level Set Methods and Dynamic Implicit Surfaces*, New York, Springer, 2003.

[23] S. Osher and F. Santosa, *Level set methods for optimization problems involving geometry and constraints.* I. *Frequencies of a two-density inhomogeneous drum*, J. Comput. Phys., 171 (2001), pp. 272–288.

[24] M. Persson, D. Bone, and H. Elmqvist, *Total variation norm for three-dimensional iterative reconstruction in limited view angle tomography*, Phys. Med. Biol., 46 (2001), pp. 853–866.

[25] C. Popa and R. Zdunek *Kaczmarz extended algorithm for tomographic image reconstruction from limited data*, Math. Comput. Simulation, 65 (2004), pp. 579–598.

[26] A. G. Ramm and A. I. Katsevich, *The Radon Transform and Local Tomography*, CRC Press, Boca Raton, FL, 1996.

[27] R. M. Ranggayyan, A. T. Dhawan, and R. Gordon, *Algorithms for limited-view computed tomography: An annotated bibliography and a challenge*, Appl. Optics, 24 (1985), pp. 4000–4012.

[28] M. Rantala, S. Vänskä, S. Järvenpää, M. Kalke, M. Lassas, J. Moberg, and S. Siltanen, *Wavelet-based reconstruction for limited angle X-ray tomography*, IEEE Trans. Med. Imaging, 25 (2006), pp. 210–217.

[29] F. Santosa, *A level-set approach for inverse problems involving obstacles*, ESAIM Control Optim. Calc. Var., 1 (1996), pp. 17–33.

[30] K. Sauer, S. James, Jr., and K. Klifa, *Bayesian estimation of 3-D objects from few radiographs*, IEEE Trans. Nucl. Sci., 41 (1994), pp. 1780–1790.

[31] J. A. Sethian, *Level Set Methods and Fast Marching Methods*, Cambridge University Press, Cambridge, UK, 1999.

[32] R. E. Showalter, *Monotone Operators in Banach Space and Nonlinear Partial Differential Equations*, AMS, Providence, RI, 1997.

[33] S. Siltanen, V. Kolehmainen, S. Järvenpää, J. P. Kaipio, P. Koistinen, M. Lassas, J. Pirttilä, and E. Somersalo, *Statistical inversion for medical x-ray tomography with few radiographs:* I. *General theory*, Phys. Med. Biol., 48 (2003), pp. 1437–1463.

[34] K. T. Smith and F. Keinert, *Mathematical foundations of computed tomography*, Appl. Optics, 24 (1985), pp. 3950–3957.

[35] B. Song and T. F. Chan, *Fast Algorithm for Level Set Segmentation*, UCLA CAM Report 02-68, University of California, Los Angeles, CA, 2002.

[36] J. S. Suri, K. Liu, S. Singh, S. N. Laxminarayan, X. Zeng, and L. Reden, *Shape recovery algorithms using level sets in 2-D/3-D medical imagery: A state-of-the-art review*, IEEE Trans. Inf. Technol. Biomed., 6 (2002), pp. 8–28.

[37] R. Villegas, O. Dorn, M. Moscoso, M. Kindelan, and F. J. Mustieles, *Simultaneous characterization of geological shapes and permeability distributions in reservoirs using the level set method*, in Proceedings of the SPE Europec/EAGE Annual Conference and Exhibition, Vienna, 2006, pp. 1–12.

[38] R. L. Webber and R. A. Horton, *Method and System for Creating Three-Dimensional Images Using Tomosynthetic Computed Tomography*, U.S. Patent 6,289,235, Wake Forest University, Winston-Salem, NC, September 11, 2001.

[39] R. L. Webber, R. A. Horton, D. A. Tyndall, and J. B. Ludlow, *Tuned-aperture computed tomography (TACT). Theory and application for three-dimensional dento-alveolar imaging*, Dentomaxillofac. Radiol. 26 (1997), pp. 53–62.

[40] R. T. Whitaker and V. Elangovan, *A direct approach to estimating surfaces in tomographic data*, Med. Image Anal., 6 (2002), pp. 235–249.

[41] F. Xu and K. Mueller, *RapidCT: Acceleration of 3D computed tomography on GPUs*, in Proceedings of the ACM Workshop on General-Purpose Computing on Graphics, 2004, p. C-13.

[42] D. F. Yu and J. A. Fessler, *Edge-preserving tomographic reconstruction with nonlocal regularization*, IEEE Trans. Medi. Imaging, 21 (2002), pp. 159–173.